Space Weather

RESEARCH ARTICLE
10.1029/2019SW002341

Special Section:
Outcomes of the Applied Space Environments Conference, May 12-17, 2019, Los Angeles, CA

Experimental Results of Electron Method for Remote Spacecraft Charge Sensing

M. T. Bengtson[1], K. T. Wilson[1], and H. Schaub[1]

[1]Department of Aerospace Engineering Sciences, University of Colorado Boulder, Boulder, CO, USA

Abstract Remote charge sensing is a technique that can provide valuable insight into spacecraft-environment interactions, as well as enable missions that leverage electrostatic interactions between multiple spacecraft or involve docking maneuvers in harsh charging environments. The concept discussed in this paper uses a co-orbiting servicing spacecraft to measure the energies of secondary electrons or photoelectrons that are emitted from the target object with initial energies of a few electron volts. The electrons are accelerated toward the servicing spacecraft, which is at a known positive potential (relative to the target), where they are measured by an energy analyzer. Given the potential of the servicing spacecraft, the potential of the target can be accurately determined. Results are presented from experiments conducted in a vacuum chamber to investigate the touchless sensing concept. Specifically, the feasibility and accuracy of the electron method is considered for different materials, charge scenarios, and relative geometries. The results show that the surface potential of a flat plate can be accurately determined for a range of metallic surface materials, voltages, and relative angles.

M. T. Bengtson and K. T. Wilson, Graduate Research Assistants
H. Schaub, Professor, Glenn L. Murphy Endowed Chair

Key Points:
- A co-orbiting satellite can be used to measure the surface electrostatic potential of an object in space
- Experimental results demonstrate that this method is accurate for a wide range of realistic conditions

Correspondence to:
M. T. Bengtson,
mibe4496@colorado.edu

Citation:
Bengtson, M. T., Wilson, K. T., & Schaub, H. (2020). Experimental results of electron method for remote spacecraft charge sensing. *Space Weather*, *18*, e2019SW002341. https://doi.org/10.1029/2019SW002341

Received 28 AUG 2019
Accepted 14 FEB 2020
Accepted article online 18 FEB 2020

1. Introduction

Though spacecraft charging has been studied for decades, little work has been done on how to remotely sense the charge on a space object. Remote potential sensing is a concept that would enable on-orbit measurements of spacecraft surface charge, providing valuable insight into spacecraft-environment interactions. Most spacecraft do not have sensors to detect when they are charged to large potentials and at risk of arcing, which means that identifying causes of satellite anomalies is tenuous (Ferguson et al., 2014; McKnight, 2017). Many future space missions are planned that involve docking and rendezvous maneuvers in geosynchronous orbit or the outer radiation belt. For example, the National Aeronautics and Space Administration's Lunar Gateway program requires rendezvous and docking maneuvers to be carried out in the outer radiation belt. Goodman et al. (2019) show that expected conditions for docking can result in potential differences of thousands of volts between spacecraft. This creates a risk of electrostatic discharge during first contact as well as unwanted electrostatic forces and torques. Satellite operators are looking to extend the lifetime of satellites and reduce overall costs by conducting missions to service or salvage parts from old satellites (Ellery et al., 2008; Reed et al., 2016; Sullivan et al., 2013; Whelan et al., 2019). Such missions require multiple spacecraft operating in very close proximity and interfacing with each other. Similarly, Chou et al. (2019) show that there are significant risks of charging and arcing for future human missions to the lunar surface, especially in shadowed regions near the lunar poles, which have been targeting for exploration. The potentials of astronauts and other objects must be monitored and controlled to ensure mission safety and success. The ability to remotely sense the electrostatic potential on another object is critical to ensure safe proximity operations in all regions of the space environment. Additionally, numerous missions have been proposed that seek to leverage electrostatic interactions between multiple spacecraft. These concepts include the electrostatic tractor for tugging or detumbling debris objects in geosynchronous orbit (Bengtson et al., 2018; Bennett & Schaub, 2015; Schaub & Sternovsky, 2014), electrostatic inflation of structures (Stiles et al., 2013b, 2013a), and Coulomb formations (King et al., 2002). Each of these concepts would benefit significantly from knowledge of the electrostatic potential on a nearby object.

The proposed concept works by using a co-orbiting sensing spacecraft to measure the energies of electrons emitted from the target object (Bengtson & Schaub, 2019; Bengtson, Hughes, et al., 2019). Both passive and active sensing modes are possible. The active case applies to charged actuation missions, such as Coulomb formations or the electrostatic tractor, in which an electron beam is used to impose a potential on the target,

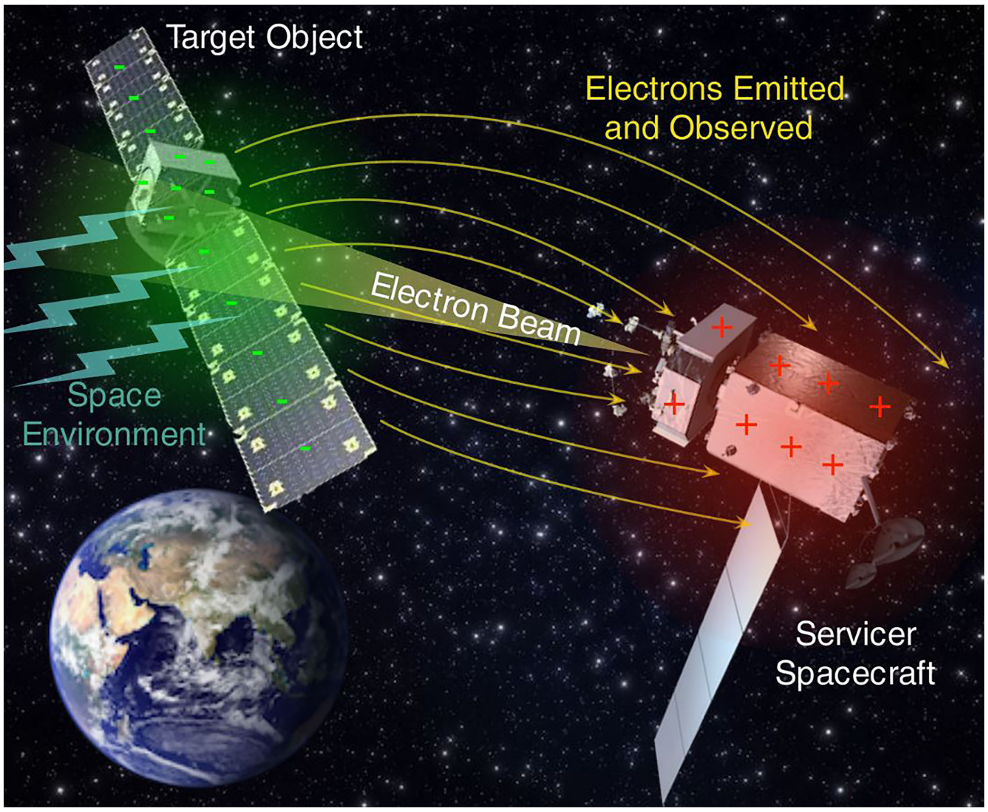

Figure 1. Concept figure showing electrons generated on a target object then accelerated toward the servicer spacecraft where they are sensed and analyzed to determine the potential of the target. Both active (electron beam) and passive (environment interactions) sensing options are depicted.

thus generating Coulomb forces and torques. The interaction of the electron beam with the target surface generates low-energy secondary electrons. In the passive sensing case, it is desired to measure the natural potential of the target, so no electron beam is used. Instead, low-energy photoelectrons or secondary electrons are generated by interactions between the target and the space environment. In both cases, the low-energy electrons are accelerated toward the sensing spacecraft, at a known positive potential, where they are measured by an energy analyzer. The final energy of the electrons is equal to the potential difference between the two craft (plus the small initial energy of the electrons). Therefore, given the potential of the sensing spacecraft, the potential of the target can be accurately determined. Figure 1 provides a concept of operations. In the active case, the electron beam is used to both force a potential on the target and generate secondaries that can be used to monitor the forced potential, enabling feedback control. In the passive case, only environmental interactions occur and the unforced potential is measured.

The same technique of observing electrons is applied to data from the Lunar Prospector mission to determine the charge distribution on the surface of the Moon and other planetary bodies (Halekas et al., 2002, 2005, 2008; Nordheim et al., 2014). Ferguson et al. (2014) propose several other methods for remotely sensing the charge on a spacecraft in orbit from the ground or another spacecraft by observing surface glows, X-ray bremsstrahlung, or radio or optical emissions from arcs. The X-ray bremsstrahlung method is another promising technique for remote charge sensing, which is discussed further in several studies (Wilson & Schaub, 2019, 2018).

This paper presents results from laboratory vacuum chamber experiments to investigate using secondary electrons and photoelectrons to touchlessly sense spacecraft electrostatic potential. The paper is outlined as follows. Section 2 provides the relevant theory and a concept of operations. Section 3 discusses the experimental design and equipment. Section 4 presents the results and discussion. Section 5 draws conclusions from the results.

2. Theory and Concept

Secondary electrons are created when an energetic electron or ion strikes a surface. The incident particle liberates electrons within the material, some of which escape the surface as secondary electrons. The initial energy distribution of secondaries has a peak at one third the work function of the material, which is about 2 eV for most surfaces (Chung & Everhart, 1974). The number of secondaries emitted for each incident particle is known as the yield, which varies as a function of the incident particle energy. It is common for materials to have a yield larger than unity for a range of incident energies. This implies that multiple secondaries are emitted for every incident particle. Above the maximum in the secondary emission yield curve, higher incident energies produce fewer secondary electrons, because the incident energy is deposited deeper in the material where electrons have a lower probability of escaping to the surface (Dekker, 1958). Secondaries are emitted with a Lambertian angular distribution about the surface normal, regardless of the incident angle of the primary particle (Bruining, 1954). Larger primary incident angles produce larger numbers of secondaries because more energy is deposited closer to the surface. Secondaries are differentiated from backscattered electrons, which are observed when the primary electron reflects off the surface.

Photoelectrons are emitted when light shines on a surface. The number of emitted electrons depends on the intensity of the light. The energy of the emitted electrons depends on the energy of the light and work function of the metal. For common spacecraft materials exposed to sunlight, photoelectrons leave the surface with energies of a few electron volts and the photoemission current is on the order of $J_{ph} = 40\mu A/m^2$. Note that this current is constant for negatively charged spacecraft and quickly vanishes as the spacecraft charge goes positive, because the photoelectrons are attracted back to the surface.

The electron method for touchless charge sensing involves two spacecraft: a target object and a sensing spacecraft. Depending on the application, the target object may be a defunct spacecraft to be salvaged or towed, a spacecraft with which another spacecraft will dock, or another active spacecraft. The sensing spacecraft flies near the target object. It is assumed that the sensing spacecraft has the ability to measure and control its own potential (Torkar et al., 2001, 2016) and can achieve a positive potential relative to the target via electron beam emission (Schaub & Sternovsky, 2014). For active sensing scenarios, in which an electron beam is used to force a potential on the target, secondary electrons are generated by interactions between the beam and the target surface. For passive sensing scenarios, in which it is desired to measure the natural target potential, photoelectrons are produced by sunlight and secondary electrons are produced by environmental currents on the target. In both cases, electrons are generated on the surface of the target object with very small initial energies of a few electron volts. The electrons are accelerated toward the sensing spacecraft, which maintains a positive potential relative to the target to attract the electrons. The sensing spacecraft uses an electron energy analyzer to measure the energy of the electron population. The energy of the electrons is equal to the potential difference between the two spacecraft (plus the small initial energy of the electrons, which is negligible compared to relevant spacecraft potentials). Therefore, if the potential of the sensing spacecraft relative to the plasma is known, the potential of the target object relative to the plasma can be inferred.

Previous analysis has investigated the expected electron signal magnitude in comparison to the background space environment currents (Bengtson, Hughes, et al., 2019). These results show that, for several representative cases, the signal magnitude is greater than or on the same order as the background magnitude. However, the signal current occurs at a discrete energy, equal to the potential difference between the two craft, whereas the background currents are distributed across a spectrum of energies. Therefore, the signal is detectable given existing sensor capabilities in a realistic space environment. Future missions will have to take care to ensure the detector design and integration onto the sensing craft is sufficient for the given mission requirements. For a general case, however, the secondary or photoelectron current emitted by the target object is sufficiently large to be measured in the geosynchronous plasma environment with separation distances on the order of tens of meters.

3. Experimental Setup

The experimental research had the following goals:

1. Demonstrate feasibility of touchless potential sensing.
2. Investigate the accuracy of the electron method for a wide range of operating conditions.

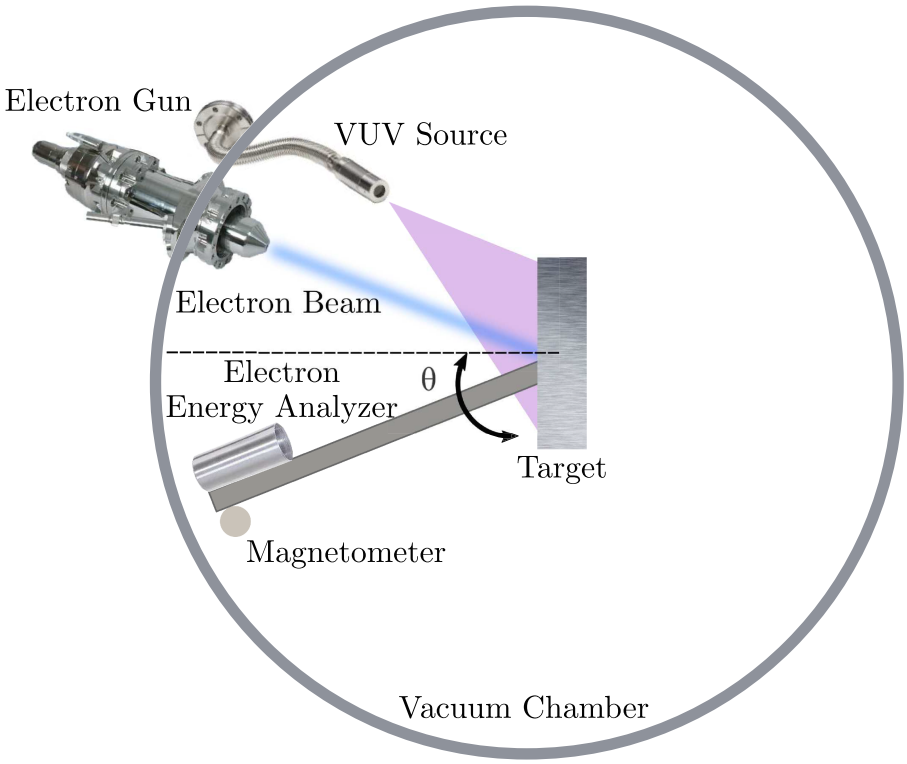

Figure 2. Schematic of the experiment setup inside the vacuum chamber. Note that the chamber walls, instrument body, electron gun chassis, VUV source, and rotating arm are all grounded (i.e., everything is grounded except for the target plate, which is held at a fixed potential).

3. Determine the effect of various target materials on the electron sensing method.
4. Determine the effect of relative geometries between the target and sensor.
5. Identify areas for future analytical and experimental research.

To achieve these goals, experiments were conducted in which a target plate was held at a fixed, known, potential in a vacuum chamber. The plate was then irradiated with either an electron beam or ultraviolet light. The resultant secondary electrons and photoelectrons were measured using an electron energy analyzer mounted on a rotating arm to sweep around the target plate. All experiments have been carried out in the Electrostatic Charging Laboratory for Interactions between Plasma and Spacecraft at the University of Colorado Boulder. The experiments consisted of a Kimball Physics EMG-4212 electron gun, a Hamamatsu L10706 vacuum ultraviolet (VUV) light source, a custom-built retarding potential analzyer (RPA) for measuring electron energy distributions, a Keithley 2401 SourceMeter, a Keithley 2301A-30-3 power supply, a Spellman CZE3000 high-voltage power supply, a Spellman SL300 high-voltage power supply, and a Matsusada CZ9 high-voltage power supply. Additionally, a Stefan-Mayer FLC3-70 magnetometer was used to measure the magnetic fields. The electron energy analyzer or RPA consists of a front grounded grid and a variable voltage discriminating grid in front of a hollow-cylinder detector. The closed-end of the hollow-cylinder detector was tapered to reduce secondary electron escape from the detector. The target plate was fixed in the center of the 0.75 m diameter bell-jar style vacuum chamber. The retarding potential analyzer and magnetometer were mounted on the end of rotating arm controlled by a rotary stage at the center of the chamber, which allowed for angular data to be collected. The angle θ is defined between the target surface normal and the energy analyzer. The electron beam has an angle of incidence on the plate of 35°. Therefore, the rotating arm could be swept over a range of $\theta = -30°$ to 90°. Experiments were conducted under a vacuum pressure between 10^{-5} and 10^{-6} torr. Target plates of various materials were used in the experiments. Materials included aluminum, copper, indium tin oxide, titanium, aluminized mylar, and Inconel. The samples were cleaned with isopropyl alcohol prior to being installed in the experiment apparatus. Figures 2 and 3 show a schematic and picture of the experimental setup, respectively.

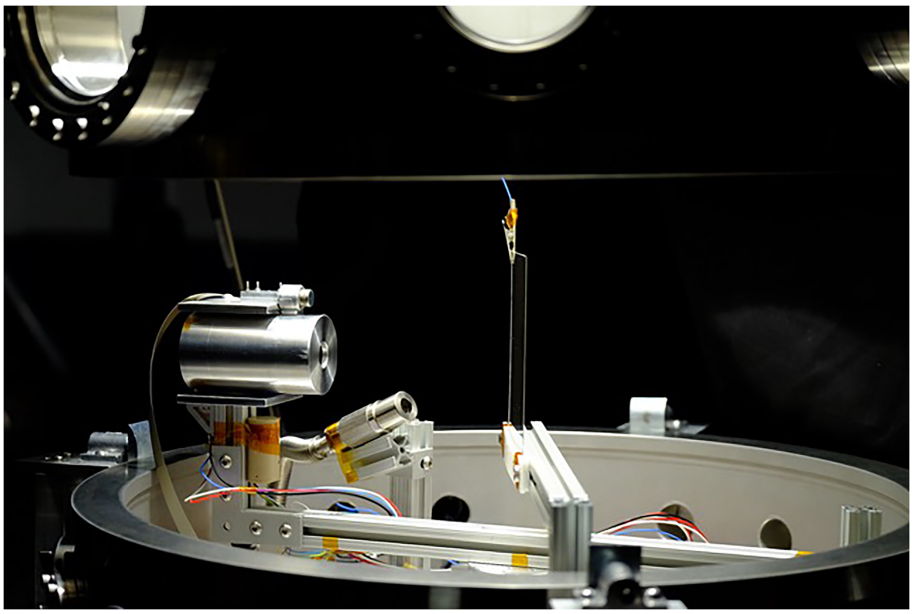

Figure 3. Experimental setup in the vacuum chamber. The target plate is at center, above the rotational stage. The electron energy analyzer is at left, mounted on the end of the rotating arm.

4. Results and Discussion

4.1. Uniform Charging

4.1.1. Example Results

Over 580 data points were collected in the experimental campaign for plate voltages ranging from −15 to −3,000 V (Bengtson, Wilson, et al., 2019). At each voltage, the electron energy analyzer was swept around the plate from −30° to +90°, where the angle θ is defined so that the plate normal is at 0° as shown in Figure 2. The angle is defined positive in the counterclockwise direction. When the instrument is closest to the electron beam, $\theta = -30°$. When the instrument is farthest from the electron beam, $\theta = +90°$. Targets were irradiated with either an electron beam or ultraviolet light. Electron beam currents ranged from 10–110 μA and electron beam energies ranged from 1.5–10 keV. Figure 4 shows results for a test in which an aluminum target plate charged to −1,000 V was irradiated by an electron beam current of 10.4 μA at an energy of 8.0 keV, simulating the active sensing case in which an electron beam is fired at the target. The electron energy analyzer was located at an angle of $\theta = 10°$. The left panel of the figure shows the electron current as the voltage on the discriminating grid is varied. As the grid voltage surpasses the voltage on the target plate (which corresponds to the energy of the secondary electrons), the current drops to 0. The right panel in the figure shows a first-order, backward-difference numerical derivative of the data and a Gaussian fit (indicated by the solid line). The actual plate potential is given by the vertical dashed line (in both panels

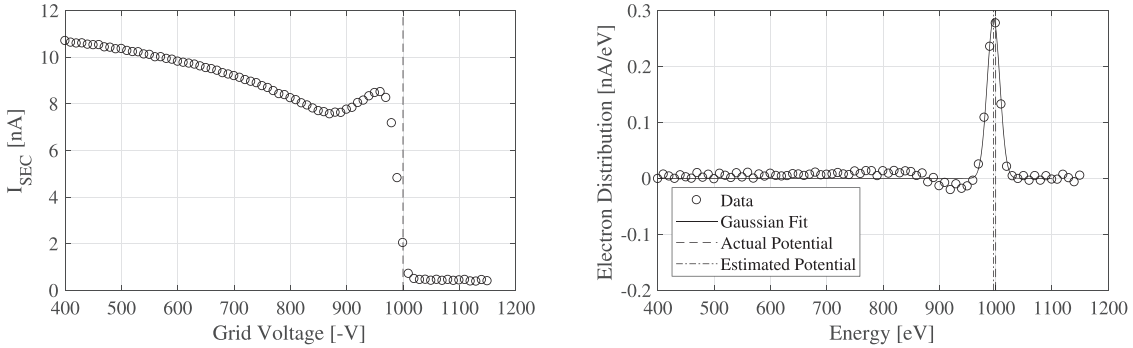

Figure 4. (left) Measured secondary electron current as a function of voltage applied to the discriminating grid for an aluminum sample charged to −1,000 V and irradiated by an electron beam. (right) Numerical derivative of the data in the left panel, which gives the electron energy distribution, Gaussian fit, actual plate potential, and estimated plate potential. The electron energy analyzer was located at an angle of $\theta = +10°$.

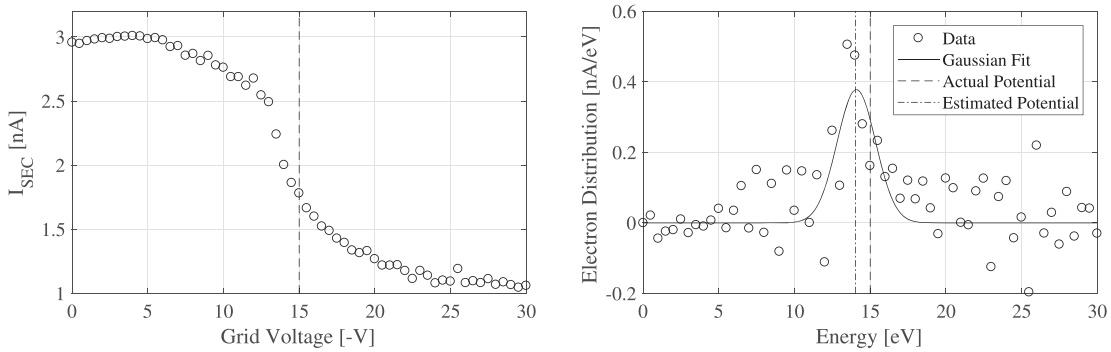

Figure 5. (left) Measured secondary electron current as a function of voltage applied to the discriminating grid for an aluminumized Kapton sample charged to −15 V and irradiated by an electron beam. (right) Numerical derivative of the data in the left panel, which gives the electron energy distribution, Gaussian fit, actual plate potential, and estimated plate potential. The electron energy analyzer was located at an angle of $\theta = 0°$.

of the figure), and the estimated plate potential is taken to be the peak of the Gaussian (indicated by the vertical dotted line in the left panel). As shown, the estimated plate potential corresponds to the actual plate potential to within the voltage step of 10 V, indicating the feasibility and accuracy of the electron sensing method for potentials in the kilovolt range.

In Figure 4 (left), a background population of electrons approximately continuously distributed in energy is present, as indicated by the approximately −0.005 nA/eV slope between 400 and 800 V. This population is likely generated when electrons from the target impact the walls or other surfaces in the vacuum chamber, thus generating other electrons. Additionally, the dip in current at 880 V is interesting. This dip was present in some, but not all, data sets. This is an artifact of backscattered electrons in the detector (Simpson, 1961). A backscattered electron is an electron that strikes a surface, then reflects off the surface with an energy up to its incident energy. Some of the secondary electrons from the target plate enter the detector, pass through the discriminating grid, then scatter off the detector surface and exit the detector. As the grid voltage approaches the energy of the secondary electrons from the target plate, the electrons that backscatter in the detector no longer have sufficient energy to penetrate the grids on the way back out. Therefore, the backscatter current is reduced and the total detected current increases as the grid voltage approaches the plate voltage.

Another representative result is shown in Figure 5, which illustrates the electron sensing method at low charging levels. In this case, a sample of aluminized Kapton is held at a potential of −15 V and irradiated with an electron beam current of 44.7 μA at an energy of 1.5 keV. The electron distribution raw data are noisy, but the secondary electron population at 15 eV is identified by Gaussian fitting routine, and the plate potential is estimated accurately. In theory, the accuracy of the technique is limited by the initial energy distribution of the electrons. Further, local surface variations or coatings can further widen the initial energy distribution, so the method is only accurate to within several volts. Therefore, at voltages near 0, the method produces larger percent uncertainties. However, small voltages are less of a concern because it is large voltages that lead to arcing or produce significant Coulomb forces and torques. Though a target in space irradiated with an active electron beam would likely charge to larger (magnitude) potentials, the low-voltage results are included here to demonstrate the sensing technique over a range of potentials.

Figure 6 shows results for an Inconel plate held at −500 V and irradiated by a vacuum ultraviolet light to simulate exposure to sunlight in space. The emitted photoelectrons are used to measure the potential on the plate very accurately. This result shows that the proposed technique is feasible for touchlessly sensing the potential of an object in space using either photoelectron or secondary electrons. Given a target in space that is irradiated with an electron beam and exposed to sunlight, both photoelectrons and secondary electrons would be emitted from the target object simultaneously, contributing to an even larger signal. Similarly, ambient electron currents produce additional secondary electrons, which could allow for passive sensing, even in eclipse.

4.1.2. Data Processing Technique

Several techniques were considered for estimating the plate potential from the raw data. One option is to fit the raw current versus voltage data with a hyperbolic tangent function, which is an analytical approximation of a step function. An analytical approximation of a step function is desirable because the ideal

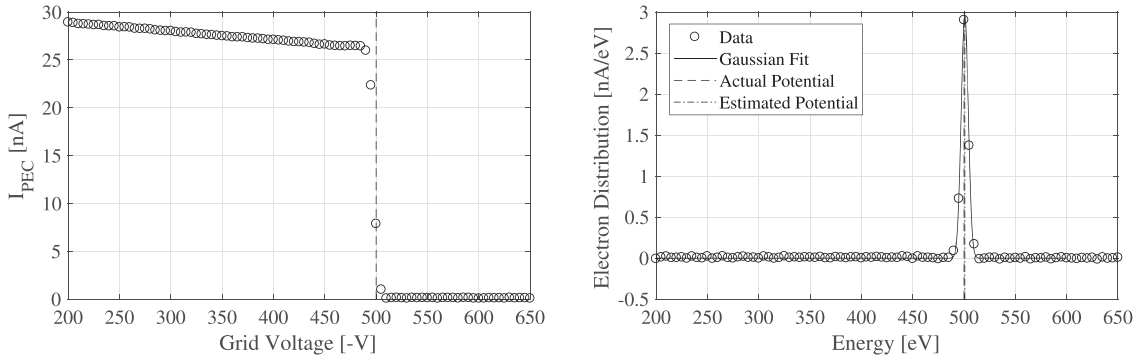

Figure 6. (left) Measured photoelectron current as a function of voltage applied to the discriminating grid for an Inconel sample charged to −500 V and irradiated by a VUV light. (right) Numerical derivative of the data in the left panel, which gives the photoelectron energy distribution, Gaussian fit, actual plate potential, and estimated plate potential. The electron energy analyzer was located at an angle of $\theta = -10°$.

current-voltage curve produced by the RPA should resemble a step function with the step occurring at the energy of the electron population coming off the plate. The negative derivative of the hyperbolic tangent function gives the electron energy distribution, and the plate potential estimate is found by taking the maximum of the electron energy distribution. This option works reasonably well except that in many cases there is a small background distribution of electrons. It is likely that the background distribution consists of secondary or backscattered electrons generated from other surfaces inside the chamber, though this will be investigated in future experiments. As a result, the current-voltage curve has a background slope that negatively affects the fit of the hyperbolic tangent function. To account for the slope, it is possible to use a fitting function, which is a hyperbolic tangent plus a linear fit. This approach models some cases quite well but breaks down when the background is flat or when the signal is very small. Additionally, the iterative least squares fitting routine is sensitive to the initial guess, which is undesirable.

Another approach is to directly compute the numerical derivative, which gives the electron energy distribution. For cases in which the electron current is much larger than the noise floor of the detection system, a clear peak is visible in the electron energy distribution (as is seen in Figures 4 and 6, right) which can be used as the plate potential estimate. However, the electron peak is lost for cases where the signal is on the same order as the system noise. In the right panel of Figure 5, for example, the peak of the numerical derivative is only slightly higher than the noise. Rather than simply taking the maximum of the electron energy distribution, a Gaussian curve is fit to the electron energy distribution. The peak of the Gaussian fit is then taken as the estimate of the target potential and the width of the Gaussian fit provides a metric for quantifying uncertainty. This data processing technique allows for accurate potential estimation which is robust even for small signals or cases in which a background distribution is present.

4.1.3. General Results

Each of the 583 tests consists of a current-voltage curve collected at a given angle, θ, and a given plate voltage and material. The peak of the Gaussian fit to the electron energy distribution for each test is found and taken as the plate voltage estimate. This estimate is then compared to the actual plate voltage and a percent error is computed. Figure 7 shows the percent error as a function of the angle θ for all 583 tests. The plot indicates the mean percent error and standard deviation of the distribution of all tests at a given angle. The means are very close to 0% error for angles ranging from −20° to 60°. The standard deviations are smallest for angles between 0° and 60°. These results indicate that the electron sensing method is accurate to within a few percent error over a range of angles centered about the surface normal. At large angles, the method becomes less reliable, but the means of the percent errors across all runs are still within 16%. Several factors contribute to this result. Interestingly, the maximum current for the electron gun experiments is not observed at an angle of 0, but rather when the detector is between 30° and 50° off the plate normal. However, for the experiments conducted with the VUV light, the maximum current is observed when the detector is near the normal angle. Figure 8 shows the current as a function of angle for several tests. The current at each

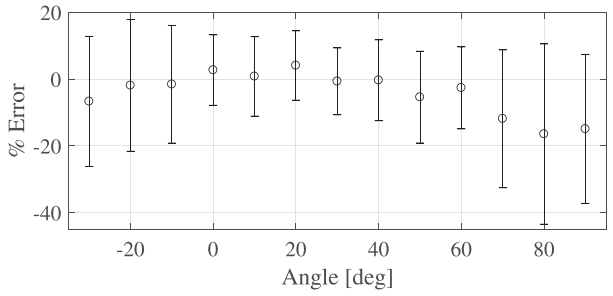

Figure 7. Percent error as a function of angle.

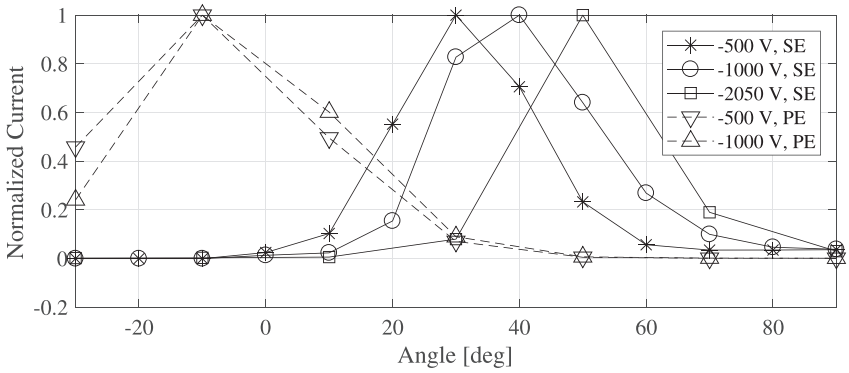

Figure 8. Normalized mean current as a function of angle. SE denotes secondary electrons, and PE denotes photoelectrons.

angle is averaged over grid voltages less than the plate voltage and then normalized. The dashed lines in the figure indicate tests in which the VUV light was used to generate a photoelectron current, whereas the solid lines indicate tests conducted with the electron gun and secondary electrons. As the plate voltage is increased for a given beam energy, the angle of maximum current shifts to higher angles. However, the maximum current for tests with photoelectrons and no beam occurs close to 0. Figure 9 shows an illustration of how the beam interacts with the target plate. If the beam energy is much greater than the voltage on the plate, then the beam electrons are unaffected by the plate until they impact it. In the extreme case in which the plate voltage is greater than the beam energy, the beam is deflected because the electrons cannot climb the potential hill to reach the plate. For cases in which the plate voltage is a fraction of the beam energy, the beam is deflected a small amount and impacts the plate closer to the edge. Due to the electric field geometry, indicated by the black arrows in the figure, secondary electrons generated closer to the edge of the plate fly away at an angle. Therefore, as the plate voltage is increased (in the negative sense), the beam is deflected further toward the edge of the plate, the resultant secondary electrons fly off the plate at an angle, and the maximum current is measured at increasingly large angles. This phenomenon is confirmed by observation of radiation darkened spots, which developed on the target plates after extended electron beam exposure. The spots were not located at the center of the plates but, instead, were offset toward the edge. The VUV light is unaffected by the plate voltage. Thus, the maximum photoelectron is always measured at an angle near the plate normal.

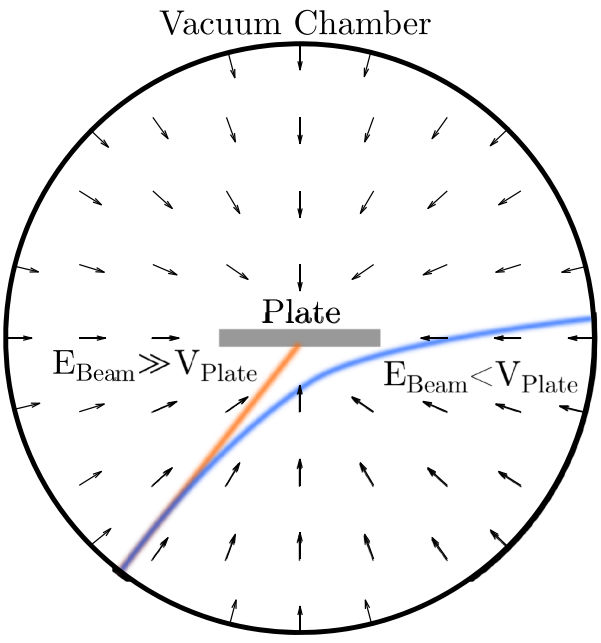

Figure 9. Schematic of the electron beam interacting with the plate. The orange line indicates a beam of energy much greater than the plate voltage. The blue line shows how the beam is deflected if the plate voltage exceeds the beam energy. Black arrows indicate the direction of the electric field around the plate.

This geometry has important implications for future touchless sensing missions. For any physical object that is charged to a negative potential (negative relative to the servicing spacecraft, which aims to capture the emitted electrons), there always exists a point on the surface for which the electric field maps to the servicing spacecraft. The electron beam can be expanded to illuminate the entire target, which ensures that some number of secondary electrons are always detected, regardless of the relative geometry of the spacecraft. Similarly, photoelectrons can always be detected by a servicing spacecraft, which observes the sunlit side of the target object, but are not detected if the servicing spacecraft is on the dark side of the target. Alternatively, if electrons are only generated on a small area of the target surface, potential measurements are possible when the relative geometries between the target and servicer are appropriate to guide the electrons to the sensor (i.e., when the target surface faces the detector). In many cases, the target may be tumbling at a high rate, whereas the target potential evolves slowly in time. Therefore, measurements are obtained at a useful rate and the potential of the target can be accurately determined. The best case scenario is when the servicing

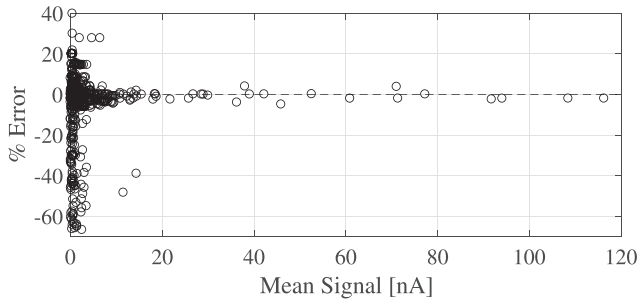

Figure 10. Error as a function of signal magnitude.

craft is using an electron beam for active sensing and is also observing the sunlight side of the spacecraft. Both secondaries and photoelectrons are generated in this case, producing a large signal. These results are especially important considering that most defunct spacecraft have complex shapes with multiple solar panels, antennas, and appendages and are generally tumbling.

Returning to the discussion of the error distributions in Figure 7, it is clear in light of Figure 8 that the signal magnitudes decrease significantly at angles beyond 60°. As the magnitude of the peak in the electron distribution approaches the noise floor of the detection system, it becomes impossible to accurately estimate the target potential. Figure 10 shows the errors plotted as a function of signal magnitude. All of the tests that resulted in large percent errors had an average signal of less than 20 nA, and the vast majority of these cases had an average signal of less than 5 nA. Several control tests were conducted in which neither the electron beam or VUV light was active, so there was no source of electrons in the vacuum chamber and the noise floor of the measurement system could be quantified. The measured noise current has a mean of 0.0124 nA and a standard deviation of 0.0339 nA. Therefore, it becomes difficult to differentiate the peak in the electron distribution from the noise as the signal magnitude approaches single nanoamps. However, for signal magnitudes on the order of tens of nanoamperes, the electron sensing method produces an estimate of the target voltage accurate to within 4%. Several sources contribute to the differences between the estimated and actual plate potentials, even when the signal magnitude is large. First, it is assumed that the discriminating grid inside the retarding potential analyzer produces a uniform, equipotential region of potential. Ideally, for a grid potential of V, only particles with energies $E > qV$ can penetrate the potential barrier. However, the wires that comprise the discriminating grid have finite dimensions and the regions between the wires have potentials slightly lower than the potentials on the actual wires (Enloe, 1994). This results in a broadening of the electron peak given by the following expression:

$$\left(\frac{\Delta E}{E}\right)\text{width} = 1 - \frac{2\pi\left(\frac{d}{a}\right) - \ln 4}{2\pi\left(\frac{d}{a}\right) - 2\ln\left[2\sin\left(\frac{\pi r}{a}\right)\right]}, \tag{1}$$

where E is the energy of the electron, ΔE is the erroneous increase in the width of the peak, r is the wire radius, a is the distance between the wires in the grid, and d is the distance between grids. For the retarding potential analyzer used in the experiments, the wire radius is on the order of 0.01 mm, the distance between wires is 0.3 mm, and the spacing between the grounded grid and discriminating grid is 10 mm. This gives a $\frac{\Delta E}{E}$ of 2.1%. Given a plate voltage of 1,000 V, the expected broadening of the peak would then be 21 eV. The electron energy distribution given in the right panel of Figure 4 has a full width at half maximum peak width of approximately 28 eV, which is consistent with this source of error. It is also not expected that the secondary electron population be monoenergetic, as secondary electrons depart from a surface with a distribution of kinetic energies of a few electronvolts. The peak of this distribution occurs at an energy equal to one third the work function of the emitting surface (Chung & Everhart, 1974).

Another consideration for planar-type retarding potential analyzers is that the energy filter only acts upon particles in the direction along the axis of the instrument (i.e., normal to the grids). The velocity of the particle in the transverse direction is unchanged. Therefore, a shift in the measured energy can occur if particles are not traveling through the device on a trajectory parallel to the instrument axis (Enloe, 1994). This shift is equal to

$$\left(\frac{\Delta E}{E}\right)\text{shift} = \sin^2\alpha, \tag{2}$$

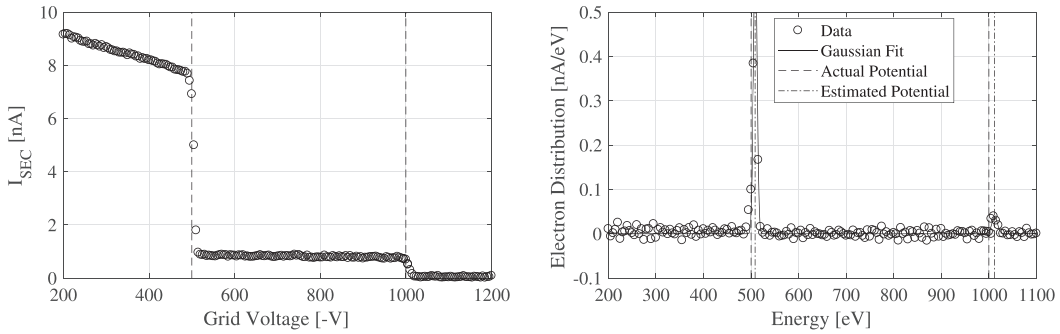

Figure 11. (left) Measured secondary electron current as a function of discriminating grid voltage for two aluminum samples charged to −500 and −1,000 V then irradiated by an electron beam. (right) Numerical derivative of the data in the left panel, which gives the electron energy distribution, double Gaussian fit, actual plate potential, and estimated plate potential. The electron energy analyzer was located at an angle of $\theta = -50°$.

where α is the angle of incidence. Two effects could cause the particles to enter the detector at an angle: (1) gyrorotation about the magnetic field and (2) misalignment of the instrument relative to the plate. The instrument is designed such that the maximum angle, α, that a particle could have and still pass through the detector is approximately 25°. This gives a $\frac{\Delta E}{E}$ shift of 18%.

Finally, the presence of oxide layers or other contaminants on the surface of the target material can produce localized surface potential variations on the order of hundreds of millivolts (Robertson et al., 2004). There were no significant differences observed between the different materials tested, which encompass a variety of common spacecraft materials including metals, solar panel coverglass, and thermal insulation. Future tests will also investigate electron emission from samples of spacecraft thermal control paint.

In these experiments, the separation distance between the target plate and sensor is approximately 25 cm. Due to the finite diameter of the chamber, it is not possible to significantly increase the separation distance. For on orbit applications, however, relevant separation distances are on the order of tens of meters. Previous simulation work has shown that the signal remains above a reasonable detection threshold, even for separation distances on the order of tens of meters (Bengtson, Hughes, et al., 2019). Whereas the electric field about a charged object falls off with the inverse of the distance squared, the signal current captured at a given distance depends on the voltages of each craft. If the potential difference magnitude is small (on the order of volts of tens of volts), the initial angular distribution of the electrons causes the electron beam to expand, and thus, the signal decreases strongly as a function of distance. If the potential difference magnitude is large, however, the initial energy distribution is negligible and the signal does not decrease as strongly with increasing distance. Future simulations and experiments in larger vacuum chamber facilities are planned to further investigate the scalability of these results to larger separation distances.

4.2. Differential Charging

It is known that spacecraft do not always charge to uniform potentials (e.g., Garrett, 1981; Prokopenko & Laframboise, 1980). Differential charging occurs when various spacecraft surfaces charge to different potentials. This can occur because different materials have different charging characteristics or because different surface are exposed to different conditions. Though design guidelines recommend that all satellite surface be connected to a common electrical ground to prevent differential charging, this guideline is not always followed (Steves, 1980). For example, one side of the spacecraft has a photoelectron current because it is in sunlight, whereas the shaded surfaces do not experience photoelectron emission. An experiment was conducted to determine if the electron sensing method could accurately identify the potentials on adjacent, differentially charged surfaces. Instead of a single target plate, two target plates were placed side-by-side in the experiment apparatus such that they were electrically isolated. A different voltage was applied to each plate and the electron analyzer was swept around the target setup. Figure 11 shows the results for one such test. At this angle of $\theta = 50°$, both target potentials are sensed simultaneously, as indicated by the electron peaks at 500 and 1,000 eV. This demonstrates that electron-based remote sensing is effective even for more complex and realistic charging scenarios. The position and geometry of the targets becomes increasingly important for differential charging tests. For angles less than 50°, only the peak at 1,000 eV is observed because the −1,000 V plate was located on the left of the −500 V plate. Therefore, electrons generated on

the surface of the −500 V plate are steered further to the right and are only observed when the detector is at larger angles. In other tests, only one peak is observed at a given angle. Future experiments will consider sensing differential charging on realistic spacecraft models.

5. Conclusions

The experimental results demonstrate the accuracy of the electron remote sensing technique for a range of target materials, voltages, and geometries for fixed target voltages. It has been shown that the method is accurate to within 4% error when the signal magnitude is on the order of 10 nA or above. An important result is that the relative geometry between the target surface normal and the detector has a large impact on the signal magnitude because the electric field near the target will determine the trajectory of the electrons. Rather than using a small beam spot size, it may be advantageous to irradiate a large portion of the target surface, thereby ensuring that some of the generated electrons map to the detector.

There are several promising avenues for future research. Additional experiments will be conducted on more complex targets, such as model spacecraft with boxes, panels, antennas, and appendages. Differentially charged surfaces will be incorporated on a single target. The maximum separation distance between the target and sensor is limited due to the physical size of the vacuum chamber, so 3-D simulations will be used to model the performance of the system with realistic separation distance and target geometries. A filter will be developed to estimate the target potential over time with appropriate confidence bounds, even if the signal temporarily drops out because the target spacecraft is tumbling. Ultimately, implementing the system in real-time on an experimental test bed with a tumbling model spacecraft target will advance the technological readiness to a high level.

Acknowledgments
M. Bengtson is funded by a National Defense Science and Engineering Graduate Fellowship. The authors would like to thank Dalton Turpen for assistance in building the retarding potential analyzer and experiment apparatus. The data presented in this work are openly available on the 4TU Centre for Research Data Repository. The data are accessible with the following DOI: 10.4121/uuid:4b95c725-c78b-430f-8319-188896b1e7b3.

References

Bengtson, M., Hughes, J., & Schaub, H. (2019). Prospects and challenges for touchless sensing of spacecraft electrostatic potential using electrons. *IEEE Transactions on Plasma Science*, *47*(8), 3673–3681.

Bengtson, M., & Schaub, H. (2019). Remote sensing of spacecraft potential at geosynchronous orbit using secondary and photo electrons. In *Aiaa scitech 2019 forum* (pp. 311). San Diego, CA.

Bengtson, M., Wilson, K., Hughes, J., & Schaub, H. (2018). Survey of the electrostatic tractor research for reorbiting passive GEO space objects. *Astrodynamics*, *2*(4), 291–305.

Bengtson, M., Wilson, K., & Schaub, H. (2019). Dataset for remote spacecraft charge sensing experiments. 4TU Centre for Research Data Repository.

Bennett, T., & Schaub, H. (2015). Touchless electrostatic three-dimensional detumbling of large axi-symmetric debris. *The Journal of the Astronautical Sciences*, *62*(3), 233–253.

Bruining, H. (1954). Physics and applications of secondary electron emission.

Chou, K., Wang, A., Yu, W., & Wang, J. (2019). Laboratory experiments on dusty spacesuit charging and arcing in plasma. *IEEE Transactions on Plasma Science*, *47*(8), 3898–3904.

Chung, M., & Everhart, T. (1974). Simple calculation of energy distribution of low-energy secondary electrons emitted from metals under electron bombardment. *Journal of Applied Physics*, *45*(2), 707–709.

Dekker, A. (1958). Secondary electron emission, *Solid state physics* (Vol. 6, pp. 251–311). Elsevier.

Ellery, A., Kreisel, J., & Sommer, B. (2008). The case for robotic on-orbit servicing of spacecraft: Spacecraft reliability is a myth. *Acta Astronautica*, *63*(5-6), 632–648.

Enloe, C. (1994). High-resolution retarding potential analyzer. *Review of scientific instruments*, *65*(2), 507–508.

Ferguson, D. C., Murray-Krezan, J., Barton, D. A., Dennison, J., & Gregory, S. A. (2014). Feasibility of detecting spacecraft charging and arcing by remote sensing. *Journal of Spacecraft and Rockets*, *51*(6), 1907–1913.

Garrett, H. B. (1981). The charging of spacecraft surfaces. *Reviews of Geophysics*, *19*(4), 577–616.

Goodman, M., Paez, A., Willis, E., & DeStefano, A. (2019). An analytic model for estimating the first contact resistance needed to avoid damaging ESD during spacecraft docking in GEO. In *Applied space environments conference*. Los Angeles, CA.

Halekas, J., Delory, G., Lin, R., Stubbs, T., & Farrell, W. (2008). Lunar prospector observations of the electrostatic potential of the lunar surface and its response to incident currents. *Journal of Geophysical Research*, *113*, A09102. https://doi.org/10.1029/2008JA013194

Halekas, J., Lin, R., & Mitchell, D. (2005). Large negative lunar surface potentials in sunlight and shadow. *Geophysical research letters*, *32*, L09102. https://doi.org/10.1029/2005GL022627

Halekas, J., Mitchell, D., Lin, R., Hood, L., Acuña, M., & Binder, A. (2002). Evidence for negative charging of the lunar surface in shadow. *Geophysical research letters*, *29*(10), 77–1. https://doi.org/10.1029/2001GL014428

King, L. B., Parker, G. G., Deshmukh, S., & Chong, J.-H. (2002). Spacecraft formation-flying using inter-vehicle Coulomb forces. *NIAC Phase I Final Report*.

McKnight, D. (2017). Examination of spacecraft anomalies provides insight into complex space environment. *Acta Astronautica*, *158*, 172–177.

Nordheim, T., Jones, G., Roussos, E., Leisner, J., Coates, A. J., Kurth, W., et al. (2014). Detection of a strongly negative surface potential at Saturn's moon Hyperion. *Geophysical research letters*, *41*, 7011–7018. https://doi.org/10.1002/2014GL061127

Prokopenko, S., & Laframboise, J. (1980). High-voltage differential charging of geostationary spacecraft. *Journal of Geophysical Research*, *85*(A8), 4125–4131.

Reed, B. B., Smith, R. C., Naasz, B. J., Pellegrino, J. F., & Bacon, C. E. (2016). The Restore-L servicing mission, *AIAA space 2016* (pp. 5478). Long Beach, CA: AIAA.

Robertson, S., Sternovsky, Z., & Walch, B. (2004). Reduction of asymmetry transport in the annular penning trap. *Physics of Plasmas*, *11*(5), 1753–1756.

Schaub, H., & Sternovsky, Z. (2014). Active space debris charging for contactless electrostatic disposal maneuvers. *Advances in Space Research*, *53*(1), 110–118.

Simpson, J. A. (1961). Design of retarding field energy analyzers. *Review of Scientific Instruments*, *32*(12), 1283–1293.

Steves, N. (1980). Use of charging control guidelines for geosynchronous satellite design studies.

Stiles, L., Schaub, H., Maute, K., & Moorer, D. F. (2013a). Electrostatically inflated gossamer space structure voltage requirements due to orbital perturbations. *Acta Astronautica*, *84*, 109–121.

Stiles, L., Schaub, H., Maute, K., & Moorer, D. (2013b). Electrostatic inflation of membrane space structures. In *Aiaa/aas astrodynamics specialist conference* (pp. 8134). Toronto, Canada.

Sullivan, B., Barnhart, D., Hill, L., Oppenheimer, P., Benedict, B. L., Van Ommering, G., et al. (2013). DARPA Phoenix Payload Orbital Delivery System (PODS): FedEx to GEO. In *Aiaa space 2013 conference and exposition* (pp. 5484). San Diego, CA.

Torkar, K., Nakamura, R., Tajmar, M., Scharlemann, C., Jeszenszky, H., Laky, G., et al. (2016). Active spacecraft potential control investigation. *Space Science Reviews*, *199*(1-4), 515–544.

Torkar, K., Riedler, W., Escoubet, C., Fehringer, M., Schmidt, R., Grard, R., et al. (2001). Active spacecraft potential control for Cluster—Implementation and first results. *Annales Geophysicae*, *19*, 1289–1302.

Whelan, D. A., Adler, EA., Wilson, S. B. III., & Roesler, G. M. Jr. (2000). DARPA orbital express program: Effecting a revolution in space-based systems. In *Small payloads in space* (Vol. *4136*, pp. 48–56). San Diego, CA: SPIE International Symposium on Optical Science and Technology.

Wilson, K., & Schaub, H. (2018). Prospects and challenges of bremsstrahlung-based electrostatic potential and material composition determination for spacecraft. In *The 15th spacecraft charging and technology conference*. Kobe, Japan.

Wilson, K., & Schaub, H. (2019). X-ray spectroscopy for electrostatic potential and material determination of space objects. *IEEE Transactions on Plasma Science*, *47*, 3858–3866.